The challenge of filtering photons in a cold environment

Elena Mazzeo

Università degli Studi di Milano, Italy

September 6, 2018

Supervisors: Friederike Januschek and Axel Lindner

Abstract

This project's aim is to present measurements and simulations on experimental set-ups employed for filtering background photons in a cold environment. The main result is that signal losses observed when filtering devices are employed can be partially explained considering thermal shrinking of components.

Contents

1 The quest for axions and axion-like particles

This first section is derived from references [1], [2], and [3].

1.1 The low energy frontier for physics beyond the Standard Model

Our current understanding of the sub-atomic universe is based on the Standard Model (SM) of particle physics. The SM describes three of the four known fundamental forces (the electromagnetic, weak, and strong interactions, and not including the gravitational force) as well as classifies all known elementary particles. All matter particles (leptons and quarks) and force carries (gauge bosons) plus the Higgs boson described by the SM have been accounted for since 2012, when the Higgs boson was observed at LHC, thus providing the last building brick of the SM.
However, despite being the best description there is of the sub-atomic world, the SM is not a theory of everything: the SM is not able to explain the complete picture. The theory incorporates only three out of the four fundamental forces, omitting gravity. Furthermore, astrophysical and cosmological observations provide evidence for the existence of dark matter and dark energy, which can't be explained by the SM. Physicists have been trying for decades to extend the SM to a more general theoretical framework, which could provide explanation for dark matter phenomena.
A theory like supersymmetry is able to fulfill this aim: supersymmetry predicts the existence of very heavy particles, which could constitute dark matter. These particles are summarized as weakly interacting massive particles (WIMPs), and the development of colliders able to reach TeV energies, such as LHC, allows physicists to probe their existence [1].
However, despite the huge efforts dedicated to the search for WIMPs in colliders, no evidence for WIMPs has emerged so far.
Complementary to the searches for massive particles carried out with high energy colliders, a new field has emerged in the last decade: this field searches for light particles with a very low interacting cross section with SM particles. The existence of these extremely weakly interacting sub-eV particles (WISPs) is predicted by many SM extensions. Furthermore, these particles could be dark matter constituents and could also explain some astrophysical phenomena, like anomalous white dwarf cooling and the intergalactic propagation of very-high-energy gamma rays.
Due to their weak interaction with SM particles, WISPs' existence cannot be probed by colliders: WISPs' searches require extreme precision experiments.
ALPS II is an example of a WISP laboratory experiment, whose aim is to probe the existence of axions and axion-like particles (see next section). The main challenge for ALPS II is boosting the sensitivity: for this purpose an intense laser, long-distance resonance cavities and a single photon detector are employed. Furthermore, since the experimental search for WISPs is a very young field, one should not be surprised by many new ideas for the development of such experiments (and new challenges).

[1] WIMPs dominated the search for dark matter since the 1980s, when it was realized that the existence of massive particles with a cross section of the order of the weak interaction would result in precisely the right density to explain dark matter. This result is known as the *WIMP miracle*.

1.2 Physics case of axions and axion-like particles

1.2.1 The strong CP problem and the QCD axion

An issue that the SM is not able to address is the so called strong CP problem. The theory of quantum chromodynamics (QCD) does not exclude a CP violation in quark interactions: however, such a violation is not observed experimentally[2]
The absence of experimentally observed CP violations in strong interactions constitutes a theoretical puzzle, because there is no fundamental reason forbidding such a violation to happen, not to mention that the magnitude of this violation (which can be parametrized with an angle θ) receives a contribution from the weak sector of the SM (it is well established that weak interactions violate CP).
This constitutes nd evident fine tuning of the CP violation parameters in QCD and in weak interactions, which, for apparently no reason at all, happen to be the exact opposite of each other, so as to prevent a CP violation in strong interactions.
Peccei and Quinn solved this strong CP problem by replacing the angle θ by a dynamical field, $\theta(x)$: QCD dynamics ensures that the low-energy effective potential of this field has an absolute minimum at $\theta = 0$. The magnitude of the violation θ spontaneously acquires the equilibrium position, explaining why a CP violation is not observed in QCD (in vacuum).
Given this elegant solution of the strong CP problem, Wilczek and Weinberg noticed that the introduction of a new dynamical field $\theta(x)$ gives rise to a new particle exitation of this field. Since this particle would wash out the strong CP problem, it was named after a detergent: the axion. Because it was motivated by QCD it is also called the QCD axion. Essentially all of the physics of the QCD axion depends on a large unknown energy scale f_a, at which Peccei-Quinn symmetry[3] is broken. The mass of the axion m_a (which is finite, because the QCD axion necessarily couples to gluons) can be expressed as a fuction of f_a and the mass and the decay constant of the pion m_π and f_π:

$$m_a \approx \frac{m_\pi f_\pi}{f_a} \approx 1 \text{ meV} \times \frac{10^{10} \text{ GeV}}{f_a} \tag{1}$$

The coupling of the QCD axion to SM particle is weak if f_a is large: the magnitude of the coupling strength to photons is inversely proportional to f_a.

$$g_{a\gamma} \propto \frac{1}{f_a} \tag{2}$$

Originally, it was assumed that f_a had the same order of magnitude of the electroweak unification energy (for energies above ~ 246 GeV electromagnetic and weak interactions merge into a single electroweak interaction), but the recent experiments with colliders excluded this possibility: now f_a is believed to be larger than $\sim 10^5$ GeV. Therefore, given Eq. 1 and Eq. 2, the QCD axion must have very small mass, typically sub-eV, and feeble interactions.

[2] An example of CP conservation in strong interaction is the absence of electric dipole moment in a neutron. The neutron is a charge-neutral bound state of the three quarks udd: both u and d carry an electric charge (the charge of u and d quarks is $+\frac{2}{3}$ and $-\frac{1}{3}$). The three quarks' charges add up to zero, but there is no fundamental reason forcing the centers of the negative and positive charge distributions to coincide. However, experiments fixed an upper limit for the neutron's electric dipole moment of $\sim 3{\cdot}10^{-26}$ e cm.

[3] The introduction of a new field $\theta(x)$ is equivalent to introducing a new global symmetry.

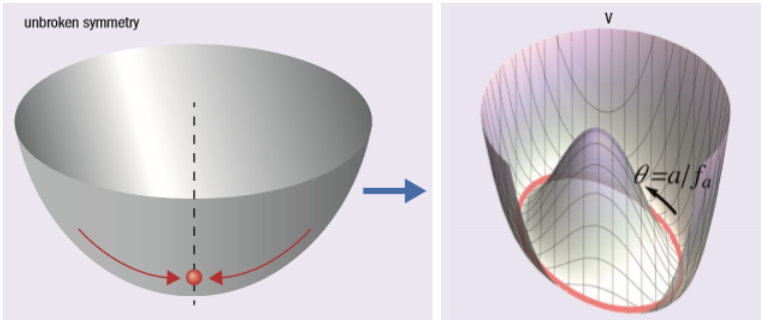

Figure 1: The potential of the field $\theta(x)$ (left) takes the form of a Sombrero (right) when this global symmetry is broken. The energy-breaking scale corresponds to the radius of the valley from the centre, while the axion represents oscillations around one of the minima. From [1].

1.2.2 Astrophysical phenomena hinting for axion-like particles

From the previous section it is evident that there is a strong physics case for the QCD axion. However, the QCD axion is only one representative of the WISP family. The case of the QCD axion can be generalized to other WISPs such as axion-like particles (ALPs). Like QCD axions, ALPs can be realized as particle oscillations of some dynamical fields, whose symmetries are broken at very high energies (of the order of f_a). ALPs' existence is well motivated by considering compactifications in string theory.
Unlike QCD axions, ALPs are not related to the strong CP problem and are not bound by the mass-coupling relation summarized by Eq. 1 and Eq. 2.
In the following, the most prominent observations and models providing motivation for ALPs existence are presented:

- **Astrophysical observations:**

  1. ALPs and, more generally, WISPs, could provide an additional cooling channel for stars. Assuming WISPs are produced in the stellar core, they could pass the outer stellar region not interacting with SM particles. This could explain the discrepancy between the luminositity of white dwarves (WD) and the models describing the cooling processes.
  2. The observed flux of very-high-energy gamma rays is higher than the expectation value. This could be explained assuming ALP-photon conversions take place in magnetic fields[4] where the very-high-energy gamma rays convert to ALPs, whose very small cross section causes them not to lose energy due to interactions with SM particles, as photons would. Afterwards ALPs convert back to photons. This mechanism would allow more very-high-energy gamma rays than expected to reach Earth, explainig the discrepancy between the observed flux of these gamma rays and the expectation value. This phenomenon is called TeV transparency.

- **Cold dark matter:** ALPs could be produced during the early universe (most likely in the post-inflationary epoch) and could explain cold dark matter. Constraining an axion's mass between 30 μeV and 10 meV, the existence of this axion could in fact explain all the cold dark matter in the universe.

[4]See the explanation of the Primakoff process in the next section.

- **String theory:** As mentioned above, string theory can includes ALP particles.

The observations and models mentioned above can constrain the existence of ALPs in certain regions of the parameter space (see Fig. 2).

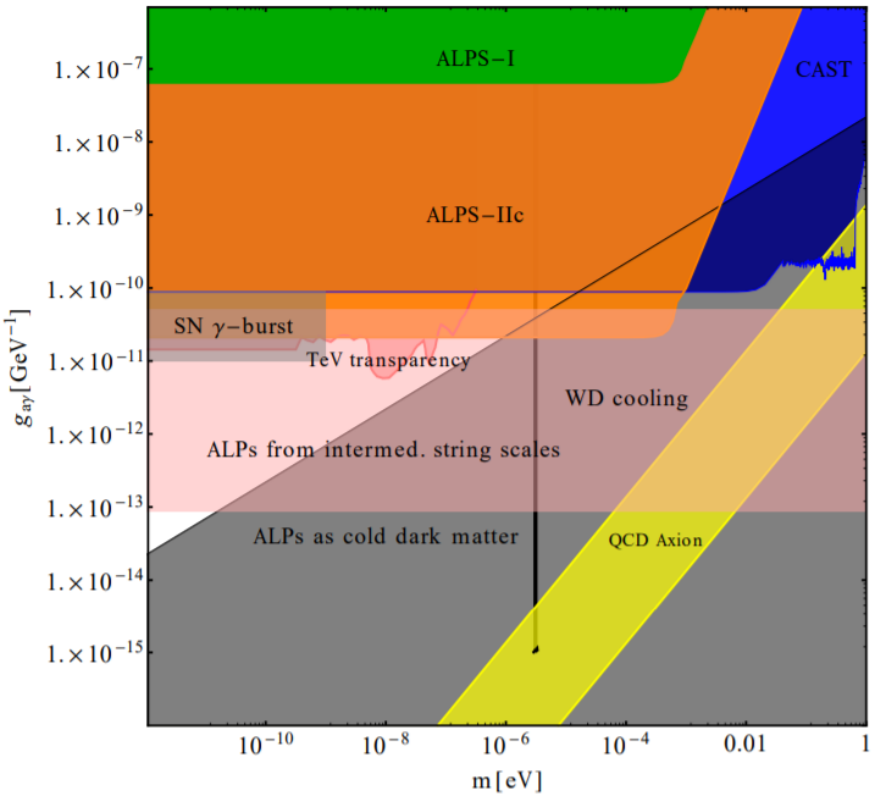

Figure 2: ALP parameter space: the parameter space is spanned by the ALP mass m_a and by the strength of the photon-ALP coupling $g_{a\gamma}$. Constraints for ALPs and QCD axion from models, experiments and observations are depicted in different colors. For comparison, the regions of the ALP parameter space probed by ALPS I and ALPS IIc are shown. From [4].

1.3 The experimental landscape

Most experiments looking for ALPs (or WISPs more in general) exploit their coupling to photons.
An axion coupling to two photons is realized through the so-called Primakoff process: an axion converts to a photon and vice versa in presence of an external electromagnetic field. This can result in photon-axion oscillations.
Assuming that the external magnetic field $\vec{B}$ is perpendicular to the photon propagation's direction, the probability of an axion converting to a photon and vice versa is

$$\mathcal{P}_{a\to\gamma} = \mathcal{P}_{\gamma\to a} \propto g_{a\gamma}^2 \cdot B^2 \cdot L^2 \tag{3}$$

where B is the external magnetic field intensity and L is the distance traveled through the magnetic field. Both the Primakoff effect and the conversion probability can be generalized to ALPs.
Most experiments search for axions and ALPs exploiting the Primakoff effect. Three

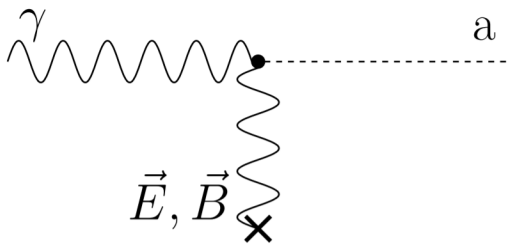

Figure 3: This diagram illustrates a photon-axion oscillation in presence of an external electromagnetic field. The diagram can be read from left to right (photon to axion) and from right to left (axion to photon).

main approaches are currently pursued: haloscopes, which look directly for dark-matter WISPs in the galactic halo of our Milky Way; helioscopes, which search for ALPs or axions emitted by the Sun; and laboratory experiments, which aim to generate and detect ALPs in a single setup.
In the following, a short overview of these three categories of experiment is presented.

Haloscopes. Axions and ALPs produce electric field oscillation in a magnetic field due to their tiny mass, which determines the frequency of these oscillations. If the de Broglie wavelength of the dark-matter axion is larger than the experimental setup, the tiny oscillations are spatially coherent in the experiment and can, in principle, be detected using a resonant microwave cavity tuned to the correct but unknown frequency. The sensitivity of such an experiment increases with the magnetic field intensity squared, the volume of the cavity and its quality factor. One drawback of this experimental set up is that, since the dark matter ALP region in the space parameter is huge (see Fig. 2), methods are required to tune the cavity to the frequency range corresponding to a certain axion mass range. Namely, this experimental set up is model dependent. This approach is carried out in the ADMX experiment [5]. A different way to exploit the tiny electric-field oscillations from dark-matter axions in a strong magnetic field is to use transitions between materials with different dielectric constants: at surfaces, the axion-induced electromagnetic oscillations have a discontinuity, which is to be balanced by radiation from the surface. The emission power does not depend on the axion mass. To boost the signal sensitivity, many magnetised dielectric discs in parallel can be placed in front of a mirror: since the emission from different surfaces is coherent, constructive interference boosts the signal sensitivity for a given frequency range determined by the spacing of the discs. The MADMAX experiment[6] follows this path, and it was demostrated that the experiment's sensitivity could be high enough to detect 100 μeV dark matter axions.

Helioscopes. ALPs with energies of the order of a few keV could be produced in the solar centre, and could be detected on Earth by pointing a strong dipole magnet at the Sun: axions entering the magnet could be converted into photons. The difference is that the Sun would emit relativistic axions with an energy spectrum very similar to the thermal spectrum in its core, so experiments need to detect X-ray photons and are sensitive only

[5]See the website https://depts.washington.edu/admx/ for further reading.
[6]See the website https://arxiv.org/abs/1712.01062 for further reading.

to some axion masses, up to a certain value depending from the spacial extension of the experiment. An example of helioscope is the CAST telescope at CERN[7].

Light shining through a wall experiments. The third approach is completely model independent, and consists in two different experimental sections. In the first section, laser light is sent through a strong magnetic field so that ALPs might be generated via interactions of optical photons with the magnetic field. The second section is separated from the first one by a light-tight wall that can only be penetrated by ALPs. These would stream through a strong magnetic field behind the wall, allowing them to be re-converted into photons and giving the impression of light shining through a wall. Thus, the detected photon rate is given by

$$\frac{dn_{detected}}{dt} = \eta \mathcal{P}_{\gamma\to a}\mathcal{P}_{a\to\gamma}\frac{dn_{produced}}{dt} \tag{4}$$

where η is the global efficiency of the set-up, $\mathcal{P}$ is the probability for ALP-photon oscillation and $\frac{dn_{produced}}{dt}$ is the rate of the laser's photons. A LSW (Light Shining through a Wall) experiment does not require any model assumption: however, the global sensitivity must be very high, since $\frac{dn_{detected}}{dt}$ is proportional to $\mathcal{P}^2 = g_{a\gamma}^4$. ALPS II experiment at DESY is the most prominent example of LSW setup: this experiment is the focus of the following section.

2 The ALPS II experiment

2.1 How to build a light shining through a wall experiment

The ALPS II experiment uses laser light to provide the photons before the wall. This offers the possibility to enhance sensitivity by implementing optical cavities[8] before and behind the wall:

- A first cavity before the wall allows to recycle the laser light, increasing the factor L in Eq. 3 and at the same time increase the light power of a power-built-up factor β_{PC}. This cavity is called *production cavity*.
- A second cavity with a power-built-up β_{RC} behind the wall enhances the probability of reconversion from ALP to photon. This cavity is called *regeneration cavity*. The regeneration cavity is able to increase the reconversion probability because the ALP's wave function behind the wall consists in a large "sterile" part and a tiny photonic component, and the photonic component is amplified by the cavity exactly like ordinary light. Since the regenerated photons in the regeneration cavity have exactly the same properties (wavelength and spacial mode) of the injected photons in the production cavity, the two cavities needs to be tuned to amplify exactly the same wavelength and spacial mode (so regenerated photons will behave in the second resonator exactly like laser light).

To exploit the Primakoff effect, two strings of superconducting dipole magnets are provided: the first one encloses the injected laser light and the second one accomodates the regeneration cavity. ALPS IIc (the third stage of the ALPS II experiment) will employ

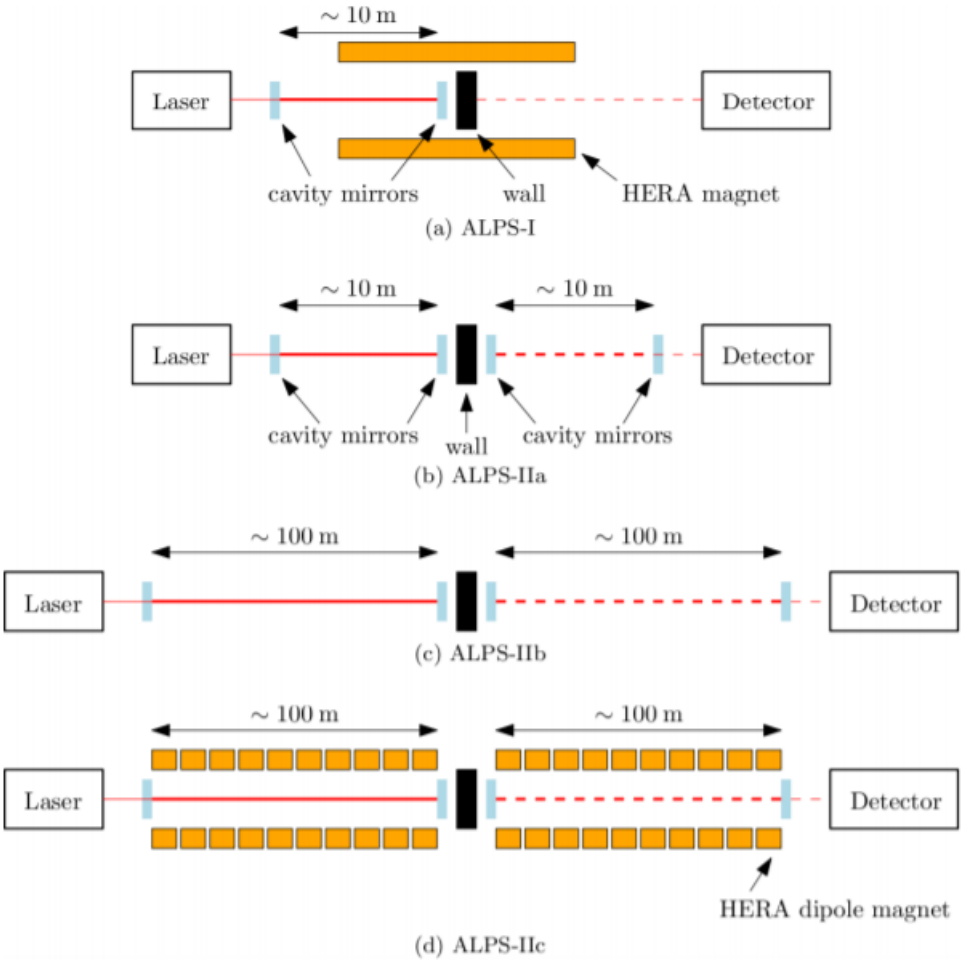

Figure 4: Schematic depiction of the experimental set-ups of ALPS I and the three stages of ALPS II. The first picture shows ALPS I's set-up: only the production cavity was employed and it incorporated a single straightened HERA magnet. ALPS IIa and ALPS IIb are intermediate stages: there are no magnets, but production and regeneration cavities are set up. The difference between these two stages is the length of the cavities: while in ALPS IIb 10 m long cavities are employed, in ALPS IIb the resonators's length will increase up to 100 m. The final ALPS II stage, ALPS IIc, will include the two strings of straightened HERA magnets. The two strings, as already pointed out, consists of ten magnets each. From [5].

two strings consisting of ten straightened HERA dipole magnets each. In addition to the described set-up, a detector for reconverted photon is needed. If the Primakoff effect takes place in ALPS IIc's set-up, the detected photon rate would be extremely small (see Eq. 4). A suitable dectector for ALPS II should be able to detect low rates of infrared single photons (approximately ~ 1 photon per day, or $\sim 10^{-5}$ photons per second) against background. The choice fell on a tungsten transition edge sensor (TES), which consists of a very tiny tungsten film, coupled to a thermal bath and to electronics for the read out, which operates in a mK-enviroment.

2.2 The optical system in ALPS II

As already pointed out in the previous section, ALPS II's optical setup mainly consists of two optical resonators (the production cavity and the regeneration cavity) and a laser. The laser wavelength is 1064 nm[9], corresponding to a photon energy of 1.165 eV: the main motivation behind the choice of this particular wavelength is that 1064 nm lasers and optical systems for 1064 nm laser beams are widely tested, used and manufactured. Furthermore, the 1064 wavelength is a good compromise between the need for a lower photon energy in order to avoid damaging the end-mirrors of the cavities and the need for a small divergency of the laser beam. To correctly understand the second limitation on the laser wavelength, one has to remember that the laser light is enclosed by a string of HERA's dipole magnets, whose aperture's diameter is 55 mm. Since in ALPS IIc set-up the laser light will travel for 100 m inside this small aperture, before being focused back by the end-mirrors, the divergency of the beam has to be small enough so that the light does not hit the dipoles' walls.
As mentioned before, in order to enhance the conversion probability, the production cavity and the regeneration cavity must be tuned to resonate with exactly the same frequency and spacial mode. Locking the two cavities together is a main challenge for ALPS II's optics collaboration. While the tuning the production cavity to amplify the 1064 nm gaussian[10] laser beam can rely to state-of-the-art tecniques in modern optics, the tuning of the regeneration cavity is a challenge. This cavity has to be kept aligned and resonant for the regenerated light without the use of any 1064 nm control light, which would overwhelm the regenerated photons' signal for the detector.
The ALPS II optics collaboration is currently testing a control system that employs 532 nm laser light[11]. Green light is injected in the regeneration cavity in order to tune it to amplify this frequency: since 532 nm is exactly half of 1064 nm, if the regeneration cavity is locked to green light there is 50% of probability that the cavity is locked to infrared light. Once this step is completed, the wavelength of the 1064 nm laser is tuned in order to be exactly twice the wavelength of the green laser: the production cavity is thus frequency locked.
Injecting green light in the regeneration cavity does not affect the detection of infrared reconverted photons: through detector calibration and data analysis infrared signal light

[7] See the website https://home.cern/about/experiments/cast for further reading.
[8] Two mirrors positioned one in front of the other constitute an optical cavity.
[9] 1064 nm light belongs to the infrared band of the electromagnetic spectrum.
[10] The spacial mode of ALPS II laser is gaussian.
[11] The 532 nm laser light has exactly twice the frequency (or half the wavelength) of 1064 nm. 532 nm belongs to the visible band of the electromagnetic spectrum and corresponds to green light.

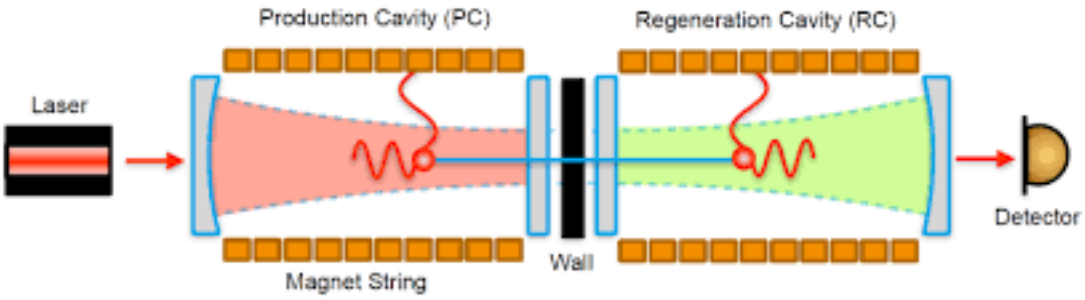

Figure 5: Drawing of ALPS IIc experimental set-up. The production cavity with the injected infrared light and the regeneration cavity with the control green light are shown. Employing a flat mirror and a focusing mirror facing the wall allows the generation of two standing waves (one in each cavity): without standing waves, there is no power-built-up in the cavities, and enhancing the conversion probability is not possible.

can be easily distinguished from the green control light[12].

2.3 The transition-edge sensor (TES) detector for ALPS II

If the Primakoff effect takes place in ALPS IIc's set-up, a rate of reconverted photons of $\sim 10^{-5}$ s^{-1} is expected. Accordingly, the main requirements for ALPS II's detector are a high detection efficiency (DE) and a low dark counts rate (DC). A further requirement is long term stability: the detector needs to be operating during the data-taking time, which is going to last six months[13]. Finally, employing a detector with good energy and time resolution is helpful for data analysis (to discriminate signal from background for example).
The ALPS II collaboration's decision was to investigate the field of cryogenic particle detection: sensors operating at very low temperature naturally show a low thermal noise, and low-noise read-out can be operated using superconducting quantum interference devices (SQUIDs).
The ALPS II's collaboration is currently testing and investigating the properties of a TES-based single photon detector. A transition-edge sensor is a calorimeter[14] which exploits the electrical resistance's strong dependence from temperature in the superconducting phase transition of the material.

Superconductivity A prerequisite for understanding how a TES detector works is knowing the basic features of superconductivity. When cooled below a certain critical temperature T_c, some conducting materials[15] undergo transition into the superconducting state, characterized by two main properties: firstly, they offer no resistance to the passage of electrical current. When resistance falls to zero, an electrical current can circulate inside a superconducting material without energy dissipation. Secondly, provided they

[12]The green control light must still be filtered as much as possible, because otherwise the detector would be saturated by 532 nm photons. However, a small leak of control light reaching the TES sensor does not spoile the signal photons' detection. From [6].

[13]The detector would not be operate continuously for six months: there would be several data-taking runs in this time.

[14]A calorimeter is a detector in which a particle's energy deposition causes a heat change in the material.

[15]It is useful to remind that the critical temperature T_c depends from the material in question.

are sufficiently weak, external magnetic fields don't penetrate superconductors, but remain at their surface. The microscopic theory of superconductivity was described by Bardeen, Cooper, and Schrieffer: according to their BCS-theory, electrons in a superconducting material group into pairs through interaction with phonons[16], forming *Cooper pairs* which move around inside the solid without friction. The energy of the electron interaction is quite weak and the pairs can be easily broken up by thermal energy (this is why BCS superconductivity occurs at very low temperature). A current formed by Cooper pairs is a supercurrent which flows with no resistance. Considering the electrical resistance as a function of temperature around the critical temperature T_c, a steep slope of the resistance occurs. As Fig. 6 shows, this resistance slope looks like an edge between the conducting and the superconducting phases. In the transition region, electrons and Cooper pairs occur both and the resistance does not follow Ohm's law anymore.

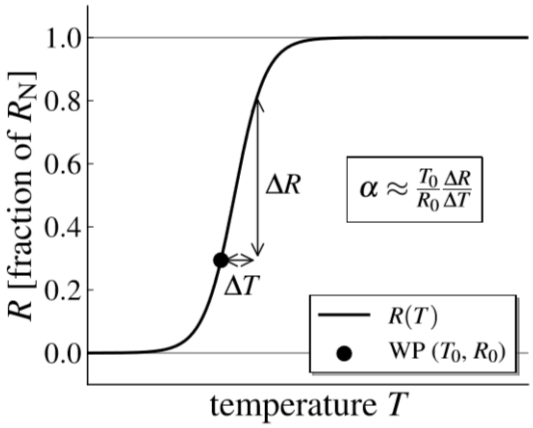

Figure 6: The electric resistance of a TES detector as a fuction of temperature is shown. R_N is the resistance of the sensor in its normal conducting phase, while WP identifies the working point of the detector. One can easily see how a small change in temperature causes a large change in resistance, if the sensor lies in the transition edge. From [4].

In the following, the working principle of a TES detector is described.
A transition-edge sensor incorporates a thermal circuit and an electric circuit. As already mentioned, the thermal circuit is a calorimeter: a sensor with heat capacity C is connected to a thermal bath with temperature T_{bath} through a thermal link with heat conductance G. The system is closed: when the thermal equilibrium is reached, the sensor has the same temperature of the bath. When an incident particle deposits an energy ΔE, the sensor heats up by

$$\Delta T = \frac{\Delta E}{C} \tag{5}$$

Because of the thermal link to the bath, the sensor cools down again. After an instantaneous heat-up of ΔT at time $t = 0$, the subsequent cool down can be described with the temperature evolution

$$T(t) \sim e^{-t/\tau} \tag{6}$$

where $\tau = \frac{C}{G}$. Measuring the deposited energy ΔE is equivalent to measuring the change in temperature ΔT: thus for particle detection it is convenient to use the TES as a

[16]The phonons are vibrations of the superconducting material's lattice.

sensitive thermometer. The TES as a thermometer benefits from a dramatic change with the temperature in electric resistance R: if the detector working point is set in the transition edge between the conducting and the superconducting phase of the sensor, a small change in temperature means a large change in resistance ΔR. Thanks to this mechanism, a TES can reach a very high sensitivity as a thermometer. How sharply the resistance changes with temperature is expressed by the temperature sensitivity

$$\alpha = \frac{T_0}{R_0}\frac{\partial R}{\partial T} \tag{7}$$

where T_0 and R_0 identify the working point of the detector.
Since setting the TES working point to the transition edge just by regulating the thermal bath temperature T_{bath} is challenging, the thermal sensor is linked to an electric circuit. If the TES is cooled and superconducting, so that $T_{bath} < T_c$, applying an external electrical current I allows to set the TES in the transition edge. In addition, an electric circuit is necessary for the read-out. A high enough current provides a breaking of Cooper pairs. This results in a state between the superconducting and normally conducting phase. The transition sensitivity referred to the current is defined by

$$\beta = \frac{I_0}{R_0}\frac{\partial R}{\partial I}\bigg|_{T_0} \tag{8}$$

Thus, the TES resistance depends on temperature and current:

$$R_{TES} = R(T, I) \tag{9}$$

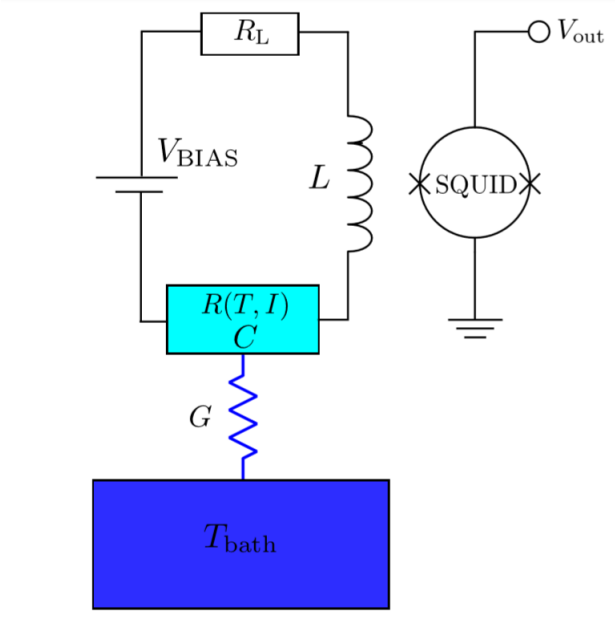

Figure 7: A TES sensor with resistance $R(T, I)$ and heat capacity C coupled with the thermal and the electric circuits is shown. The inductance L and the inductive resistance R_L allow the coupling of the TES detector with the SQUID for the read-out.

The current I_0 is provided by applying a proper constant external voltage V_{BIAS}. In the

working point, where the TES has a non-zero resistance R_0 and a certain temperature T_0, a stable equilibrium point is realized: the Joule power[17] corresponds to the power flow to the bath ($P_{J,0} = V_{TES}^2/R_0 = P_{bath}$). If the inductance L of the electric circuit (see Fig. 7) is sufficiently small, the TES voltage is constant: $V_{TES} = RI \approx V_{BIAS}$. If the TES heats up due to an external energy input (i.e. an incident photon), its resistance increases from R_0 to $R_0 + \delta R$ due to the resistance's strong dependence from the temperature in the transition edge. An increase in resistance results in a smaller Joule power ($V_{TES} = V_{BIAS} = cost.$), and thus the Joule heating is decreased. Immediately after, the TES relaxes back in the equilibrium state exchanging power with the thermal bath. This principle is called negative electrothermal feedback (negative ETF).
ALPS II's TES detector is a tungsten based transition-edge sensor. The critical temperature for tungsten is $\sim$ 100 mK: in order to operate their TES detector, the ALPS II collaboration needs a milli-Kelvin environment. ALPS II's cryostat is based on the *dilution refrigeration* principle: a dilution refrigerator (DR) is the only refrigerator system that provide continuous cooling power at temperatures below 300 mK. A DR can provide temperatures < 10 mK and operate without moving parts at the low temperature stages. A DR uses the heat of mixing of the two isotopes of helium, ^{3}He and ^{4}He, to obtain cooling. In order to be able to run the DRs cooling cycle, one should first obtain a starting temperature of about liquid helium (4.2 K) or below. ALPS II's cryostat has four different stages: the two warmest stages are cooled down to $\sim$ 37 K and $\sim$ 4 respectively by the first and the second stage of the pulse tube (PT). This pre-cooling delivered mechanically by the pulse tube allows the dilution cycle to start. The two coldest stages are cooled down with the dilution refrigeration system to temperatures of $\sim$ 0.7 K and $\sim$ 20 mK respectively. For a detailed explanation of the dilution cycle and an accurate description of ALPS II cryostat see the *Bluefors LD-series* manual. The TES detector is going to be placed on the coldest flange, and coupled with a chain of optical fibers[18]. The chain is going to convey the 1064 nm reconverted photons coming from the optical system to the cryostat, where the TES is placed. Thus, one end of the chain will have room temperature, and the other end will be cooled down at milli-Kelvin temperatures.

2.3.1 Dark counts of the TES for 1064 nm photons

A dark count is a response of a single photon detector resembling a photon signal in absence of a signal photon. The main source of dark counts for ALPS II's TES detector is thermal photons from the room temperature end of the fiber to which the TES is coupled.

As Fig. 8 shows, the black body photons emitted from the warm end of the fiber have much lower energies than the 1064 nm signal photons. However, Fig. **??** shows significant dark count rates for 1064 nm photons in three different set-ups[19] and different analysis methods: the dark event rate ranges from 10^{-3} s^{-1} up to 10^{-1} s^{-1}, while the expected reconverted photons from ALPs rate is between 10^{-5} to 10^{-4} s^{-1}. In these experimental

[17] There is a dissipated Joule power due to the finite resistance $P_{J,0} = R_0 I_0^2 = V_{TES}^2/R_0$.

[18] The final set-up will have a fiber connecting the optical system to the first stage of the cryostat. A filter for background photons will be placed there, and a second fiber will pick up the transmitted photons and bring them to the TES.

[19] For each of these three set-ups, the warm end of the fiber was at room temperature, and of course not connected to the regeneration cavity. In the set-ups 1, 2 and 3 respectively 80 cm, 157 cm and 220 cm of the fiber were in the room temperature stage of the cryostat. The remaining lengths were inside the cryostat and the cold and was connected to the TES.

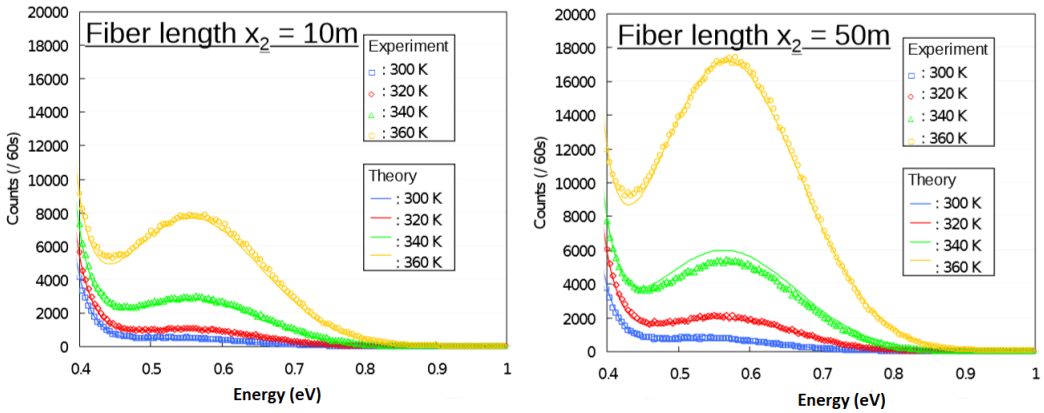

Figure 8: Thermal photon rates from different temperatures and fiber lengths are shown. A further confirmation that the rates shown are caused by black body photons it the perfect agreement of the measured rate with a model including Planck's law and fiber transmittance. It is clear that the contribution from photons with energies comparable to 1.165 eV is negligible. From [4].

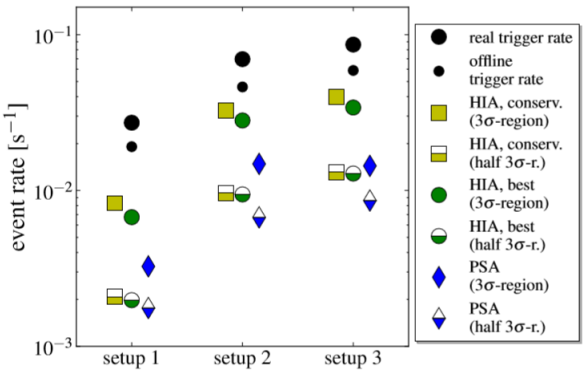

Figure 9: Dark count rates measured in three different set-ups and calculated with eight different analysis methods. From [4].

set-ups, the TES is not connected to the regeneration cavity and furthermore there is a very low population of high-energy ($\sim$ 1.16 eV) thermal photons emitted by the warm end of the fiber (see Fig. 8). However, the TES detects a non-zero rate of near-infrared photons: these signals can not come from 1064 nm reconverted photons nor from 1064 nm background photons. The explanation is that the time resolution of the TES detector is not good enough to discriminate two or more different incoming photons, hitting the detector in a tiny time window, whose energies add up to $\sim$ 1064 nm, from a single 1064 nm signal photon. This pile up of lower energy thermal photons in the TES detector overwhelms the 1064 nm signal photons. The pile up of lower energy photons is not the only possible explanation for the non-zero rate of near-infrared photons detected by the TES, but it is the most probable one. See [4] for a detailed explanation.

3 A filter for black body photons

The author's project a summer student in ALPS experiment focused on filtering low-energy photons to reduce dark counts coming from black body pile-up for 1064 nm photons of ALPS II's TES detector.
As already mentioned in the previous section, the main source of dark counts is black body radiation emitted by the room-temperature end of the optical fiber coupled to the TES detector. As Fig. 8 shows, the black body photons constituting the TES's background have lower energies than the signal photons. However, the pile-up in the TES sensor of thermal photons whose energies add up to 1064 nm boosts the dark count rate to $\sim 10^{-3} - 10^{-1}$ s^{-1} (see Fig. 9): this is at least one order of magnitude higher than the expected signal rate.
Employing a filter for 1064 nm photons could address this issue. A narrow-band filter transmitting only 1064 nm photons would stop the lower energy thermal photons to give rise to pile up in the TES's sensor. This could in principle significantly reduce the TES's dark count rates. Since the black body radiation constituting the background is emitted by the warm end of the fiber, to successfully lower the dark counts rate the filter needs to be placed inside ALPS's cryostat. The collaboration is currently also considering the option of employing a short pass filter for the same goal.
Thus, ALPS II collaboration set up a bench for a narrow-band filter. Through this filter bench, an optical fiber whose warm end is at room temperature delivers photons to the filter via a fiber-to-free space coupler incorporating a lens. The transmitted photons are then focused by a second coupler to a second fiber, which, in the final set-up, would be coupled to the TES's sensor. Since this second optical fiber would be placed in a cryogenic environment, thermal photons hitting the TES's sensor would not have sufficiently high energies to simulate a 1064 nm photon via pile-up. In principle, a very large very-low-energy photons hitting the TES's sensor at the same time could mimic a 1064 nm photon, however, the probability of this event occurring is highly suppressed. It was estimated by the ALPS II collaboration that attaching the filter bench to the lower side of the first stage of the cryostat. In fact, the lower side of the first stage of the cryostat is cooled down by the pulse tube at a temperature of $\sim$ 37 K. Wien's peak of the black body spectrum at 37 K lies at a wavelength of ~ 78.3 μm, corresponding to a photon energy of 0.016 eV[20]: a pile up of these 37 K black body photons would not significantly contribute to the dark count rates.

The filter bench set-up. As already mentioned before, the filter bench set-up incorporates two couplers, a filter, and two optical fibers going in and out. The filter and the couplers are attached to titanium holders.

- **The couplers.** The employed couplers are laser beam couplers from Schäfter+Kirchhoff. The model is 60SMS-1-4-A11-03-Ti. They are titanium couplers, and the lens has focal length of 11 mm.
- **The filter.** The filter is a narrow-band filter for 1064 nm photons from Thorlabs. The model is FL1064-10.
- **The fibers.** The fibers are singlemode fibers from Schfter+Kirchhoff. The nominal

[20]It is useful to remind that the signal photons have an energy of 1.16 eV.

Figure 10: Picture of the filter bench set-up mounted on the lower side of the first flange of the cryostat.

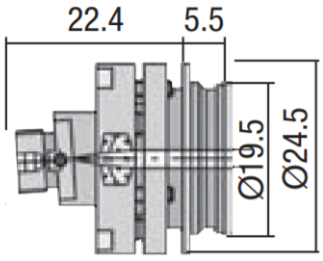

Figure 11: Drawing of one coupler. The linear dimensions are expressed in mm: thus, the total length of the coupler is 27.9 mm. From Schäfter+Kirchhoff data sheet for laser beam couplers.

aperture (NA) is 0.14 and the mode field diameter MFD is 9.8 μm[21]. The core diameter h is 8 μm. The model is SMC-980-5.5-NA014-1-APC-200. These fiber will only be used for testing: the final ALPS IIc set-up will incorporate different fibers.

3.1 Tests on different set-ups responses to a cold environment

3.1.1 Tests on the filter bench set-up

Before safely employing the narrow-band filter to lower the dark counts rate, one has to test the filter bench set-up's response to a cold environment.
The issue to address is the possibility of signal losses due to the addition of the filter bench to the experimental set-up. The theoretical peak transmittance for the filter itself

[21]The nominal aperture of the fiber coincides with the sine of acceptance angle, while the mode field diameter is the diameter of the beam profile exiting the singlemode fiber.

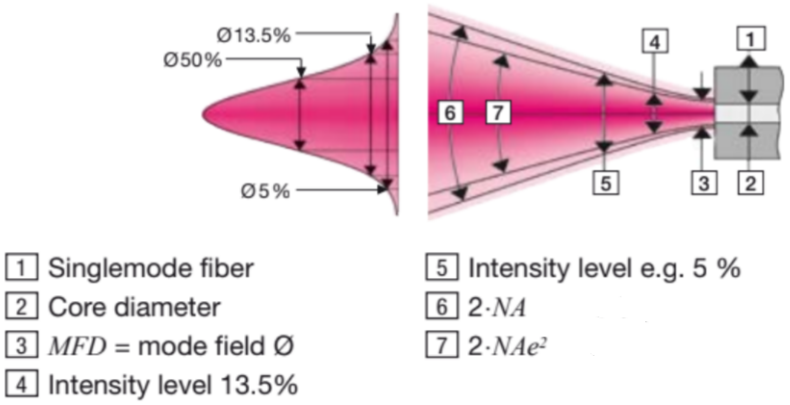

Figure 12: Drawing of a singlemode optical fiber. Some features of the gaussian beam emitted by the fiber are shown. The symbol ⊘ stands for the diameter of the beam profile. From Schäfter+Kirchhoff data sheet for optical fibers.

is larger than $\sim 80\%$, and the ultimate goal is to reach a high transmittance of $\sim 80\%$ in the cold temperature for the whole filter bench set-up. The transmittance directly affects the detection efficiency DE, which has to be maximised.
The first step to minimize signal losses is to allign the optical system. The two fibers' distance from the couplers' lenses should be as close as possible to the lenses' focal distance, and the optical axis of the system should be perpendicular to the optical elements (fibers, lenses and filter). The allignment can be performed regulating the six screws on each coupler, such that the power of the transmitted light is maximised. To carry out the allignment of the system, infrared laser light needs to be injected in the filter bench set-up: thus, measuring the injected power and the transmitted power, it's possible to calculate and maximise the system's transmittance.
The following experimental set-up allows to test the filter bench set-up's respose to the cold environment. The light from the 1064 nm **laser** is transported to a **beamsplitter** through optical fibers. The beamsplitter has four outputs: output no. 3 and no. 4 were tested and show linearity. The output no. 4 is connected to a **photodiode**, while the output no. 3 is connected to the filter bench inside the cryostat. A second fiber connects the **filter bench** to a second photodiode. The two photodiodes, respectively called Channel 0 and Channel 1, measure the injected laser power and the transmitted power through the filter bench.
Once this set-up was built, the cryostat was closed and the pulse tube delivered the first two stages of the cool down. A complete cool down with the dilution system is not needed to test the filter bench, because the set-up is placed on the first stage of the cryostat. The behaviour of the filter bench set up is also monitored during a warm up of the cryostat. During the cool down and the warm up of the environment, the laser power is not tuned by hand: however, some spontaneous oscillations are observed.
The first results of the tests on the filter bench were rather unexpected: during a warm-up, a clear anti-correlation was present between the injected laser power and the transmitted power through the filter (see Fig. 14). An anti-correlative behaviour cannot be explained by a misalignment of the system occurring due to the temperature gradient, which would rather result in an overall drop in in transmittance. In addition, an overall drop or rise in transmittance during the warm up was not observed.
During the next cool down, the observed filter bench set-up's behaviour was different:

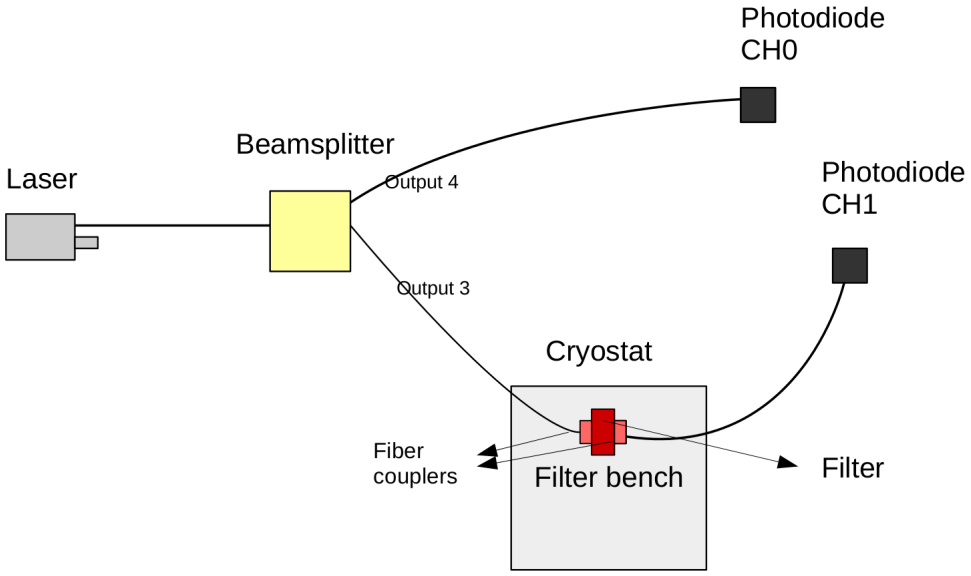

Figure 13: Drawing of the experimental set-up employed to test the filter bench set-up's behaviour.

an anti-correlation between the injected laser power and the transmitted power occurred during the first half of the cool down, until the first stage's temperature reached $\sim$ 120 K. After the temperature dropped below this value, the anti-correlative behaviour disappeared, changing to a correlative behaviour. The anti-correlation was clearly a feature of the filter bench set-up's response to a warm up and a cool down, however, a reproduceable behaviour could not be obtained.
Further tests confirmed this trend. The ALPS collaboration came up with an hypothesis on the reason for this surprising behaviour. As already mentioned before, a narrow-band filter was employed: the expected filter's transmittance is a gaussian curve centered in a wavelength of 1064 nm, with a full width at half maximum of $\sim$ 8 nm. This filter bench behaviour can be explained by assuming that the laser's emitted wavelength changes with with laser power.

3.1.2 Tests on the laser's emission spectrum

For testing the hypothesis that the employed laser had a role in the filter bench set-up behaviour, new measurements were carried out, to demonstrate a correlation between the laser's emission spectrum and the laser power.
In the following, the experimental set-up employed for these tests is described. The experimental set-up is similar to the one employed for the filter bench tests. The difference is that the output no. 3 is connected to a **spectrometer** instead of to the filter bench inside the cryostat.
The first measurements were carried out on August 14^{th}. The first observations of the laser emission spectrum showed the presence of three different emission peaks, centered respectively at a wavelength of 1059.5 nm, 1061.5 nm, 1062.7 nm. The relative area of these three peaks changed with tuning the laser power by hand. After these first observations, an experiment was carried out. First, the laser power was tuned to be close to the maximum value: this lowers the chances of the laser losing its laser properties due to

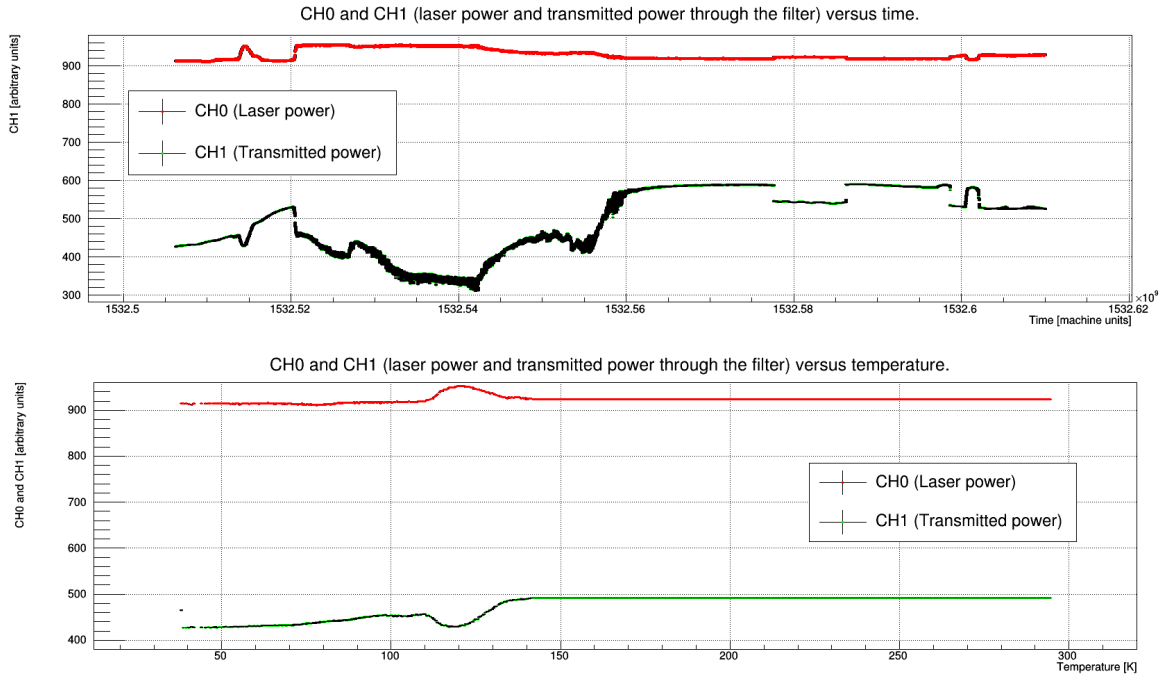

Figure 14: Injected laser power (red) and transmitted power through the filter (green) as functions of time and temperature during the warm up described before.

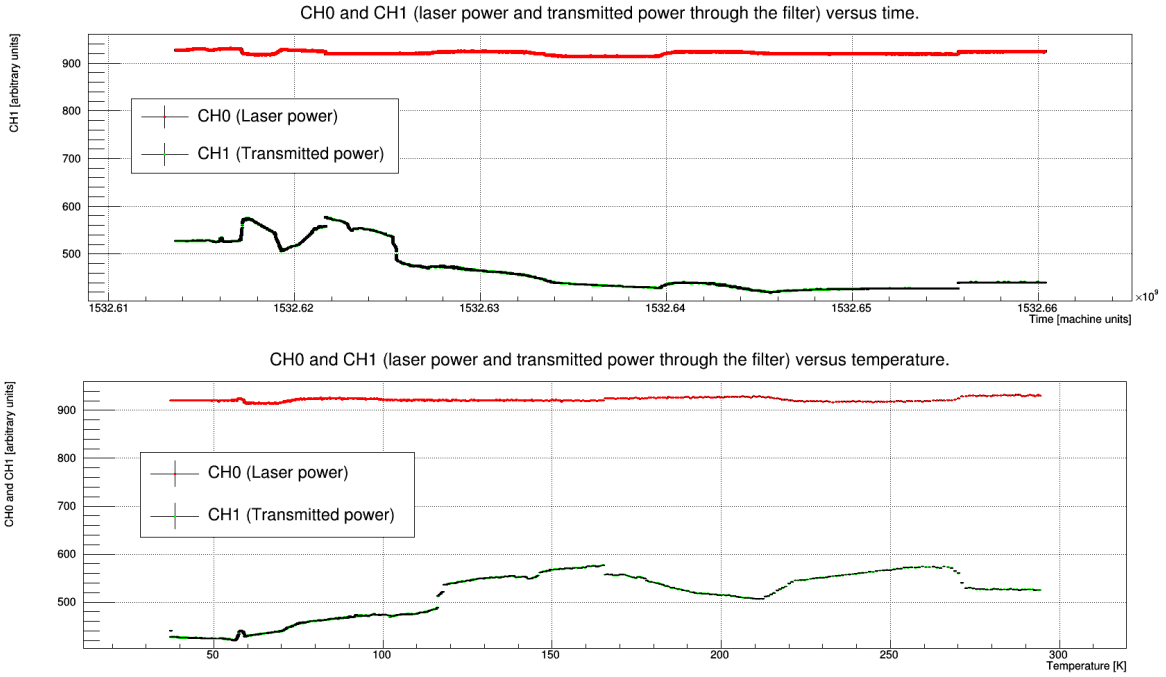

Figure 15: Injected laser power (red) and transmitted power through the filter (green) as functions of time and temperature during the cool down described before.

very low emitted power. The laser power was then not touched for two hours and at the same time laser's emission spectra were registered using the spectrometer. During these two hours of data taking, the emitted power was stable within $\sim 1\%$.
In the two following plots (Fig. 18 and Fig. 19), the experimental results are summarized.

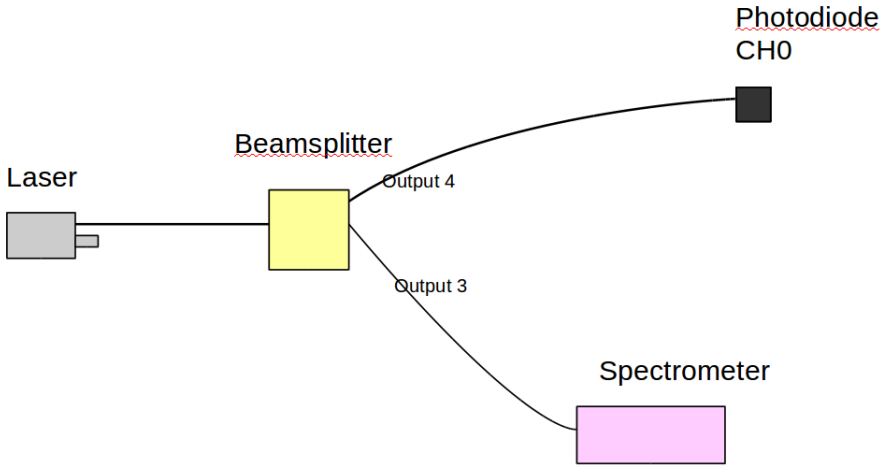

Figure 16: Drawing of the experimental set-up employed to test the laser's emission spectrum.

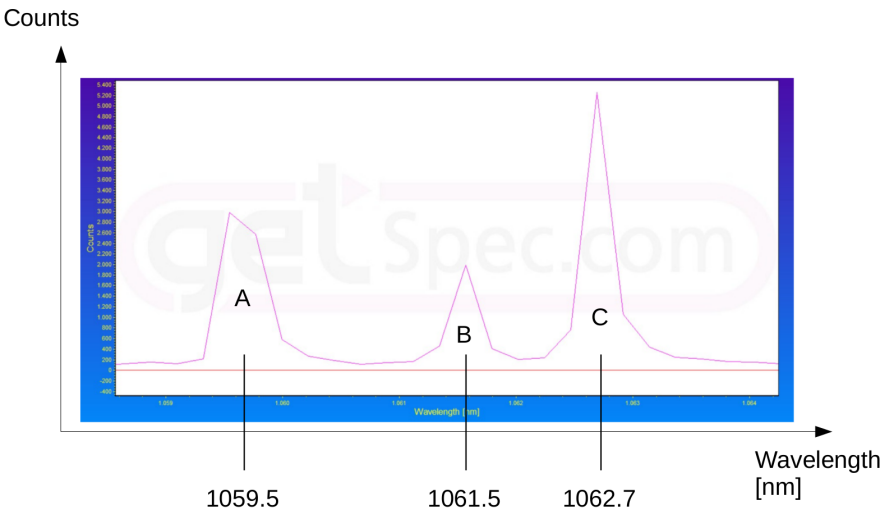

Figure 17: Example of a spectrum where the three peaks are clearly visible.

For each registered spectra, the counts under each of the three peaks were registered and plotted as function of the time of the spectrum's acquisition.

For the first half hour of data taking, the relative areas of the three peaks heavily oscillated, and for the last hour and a half the relative areas stabilized. Before carrying out the experiment, the laser had been running for many hours already: thus, the warming up of the laser played no role in the experimental outcome. The peak centered at 1062.7 nm was dominant during this time. Further tests confirmed the behaviour of the laser's emission spectrum: the laser spectrum used for the filter bench tests was not centered on a 1064 nm wavelength, and the emission spectrum changed seemingly randomly in time, without changes in the laser power. A correlation with the laser power was observed if the laser power was tuned by hand.

Testing the filter bench set-up behaviour with this laser could not lead to reliable results. The narrow band pass filter has a gaussian transmittance centered in 1064 nm with a FWHM of 8 nm. All three peaks of the laser's emission spectrum fall into this gaus-

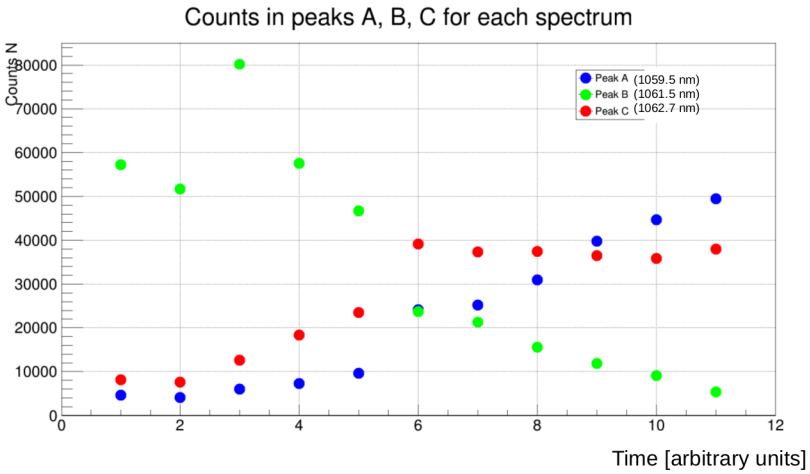

Figure 18: Counts for each of the three peaks plotted as functions of time. First half an hour of the data taking.

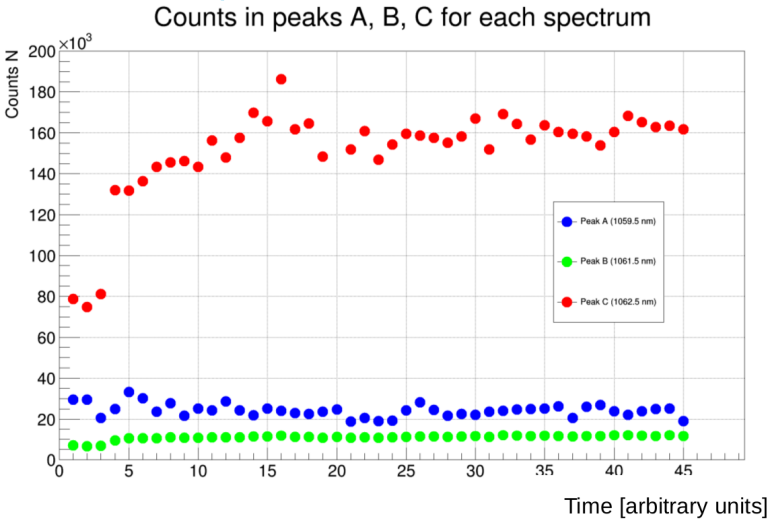

Figure 19: Counts for each of the three peaks plotted as functions of time. Second hour and a half of the data taking.

sian, but the filter transmits the wavelengths incorporated by each peak with different percentages (these percentages decrease with the distance of the considered wavelength from the peak wavelength, 1064 nm). Thus, since the relative areas of the three peaks changes with time, it is clear how an anti-correlative behaviour of the filter bench can happen. For example, if peak C's area (centered in 1062.7 nm) decreases with the laser power increasing, the overall transmittance of the set-up decreases, because there are less photons falling into the peak-area of the filters' gaussian transmittance. As a result, tests with this narrow band pass filter were discontinued.

3.1.3 Tests on optical fibers and mating sleeves

The next step focused on explaining transmittance losses observed when the filter bench set-up was employed in absence of the filter. Previous measurements revealed that a drop in transmittance from $\sim 90\%$ to $\sim 60\%$ of this value occurred during a cool down of the cryostat, when only the two couplers were mounted on the filter bench.
The ALPS collaboration was interested in ruling out a role of the optical fibers and of the

fibers' connections in this drop in transmittance.
The following experimental set-up was thus established:
The filter bench set-up was removed, and the two fibers which were previously connected to the filter bench's couplers were linked together through a Schäfter+Kirchhoff **mating sleeve**. This simple set-up was then attached with aluminium tape to the lower side of the first flange of the cryostat.
The two tests conducted with this set-up showed a drop in transmittance of $\sim$ 11% during the cool downs, and a rise in transmittance up to the room temperature value during the subsequent warm ups. This results clearly show that there is a role of the fibers or of the mating sleeves in the $\sim$ 30% drop in transmittance observed in previous measurements. Ulterior tests with a slightly different experimental set-up (two mating sleeves are placed inside the cryostat, and a **curled long fiber** connects them) show a completely different behaviour. A rise in transmittance of $\sim$ 9% occurs during the cool downs, and when the temperature of the lower side of the first stage reaches $\sim$ 60 K, a sudden jump brings the transmittance back to the room temperature value. During the warm-ups, the transmittance is stable within $\sim$ 1%.

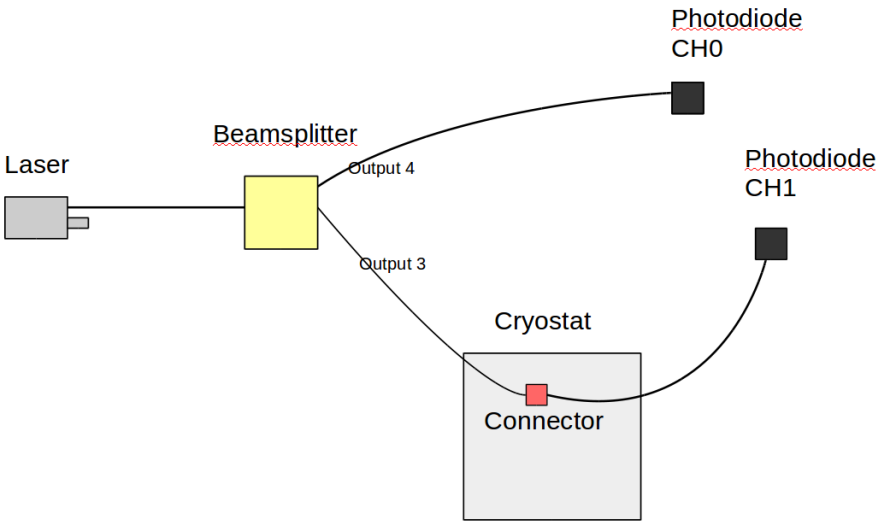

Figure 20: Drawing of the experimental set-up employed to test the behaviour of a single mating sleeve inside the cryostat.

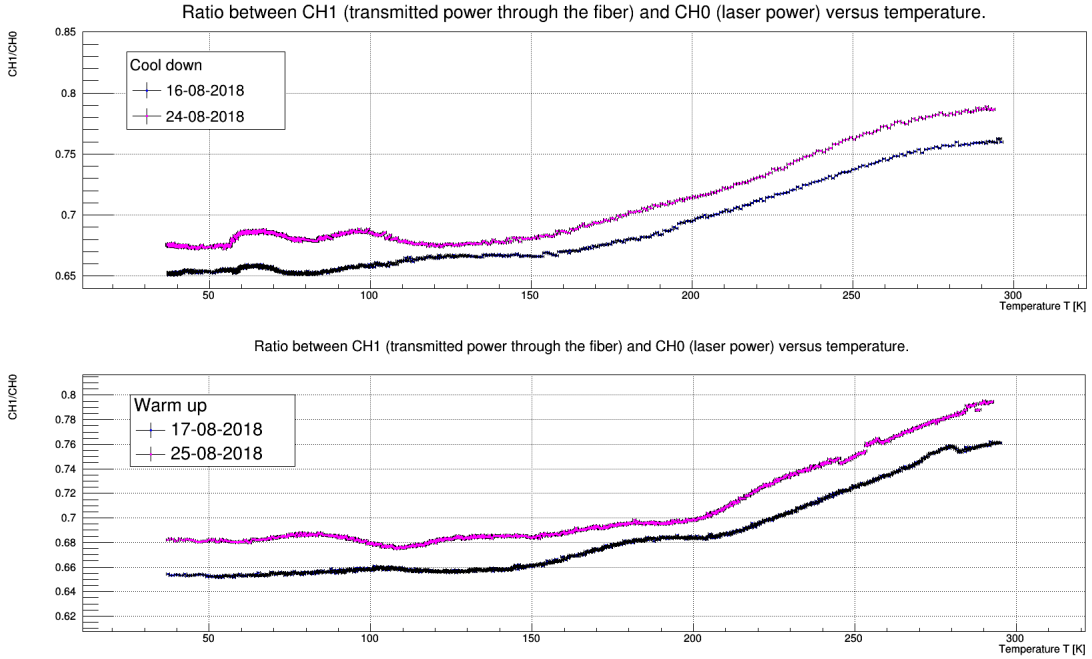

Figure 21: Transmittance of the set-up with one mating sleeve inside the cryostat during two cool downs and two warm ups plotted as a function of temperature.

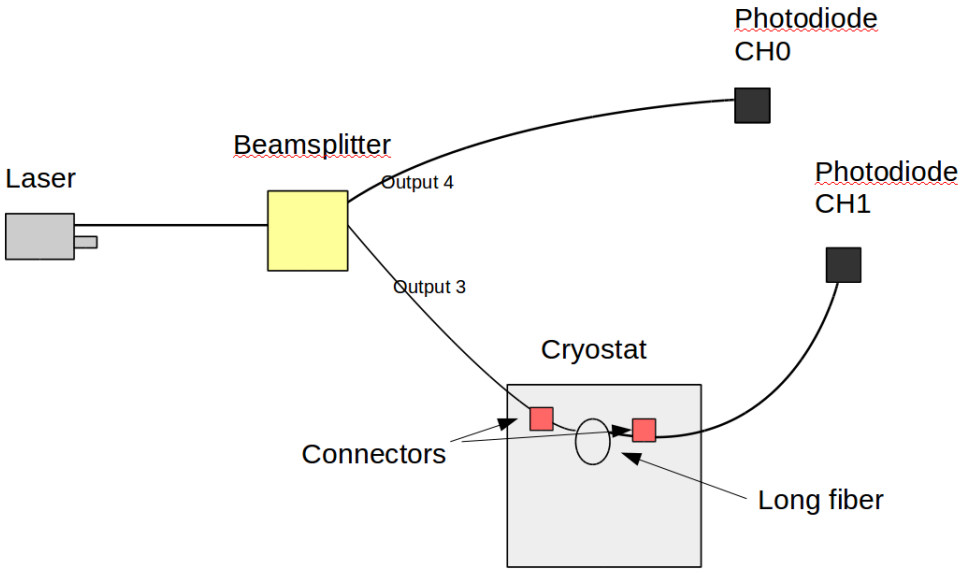

Figure 22: Drawing of the experimental set-up employed to test the behaviour of two mating sleeves connected by a curled long fiber inside the cryostat.

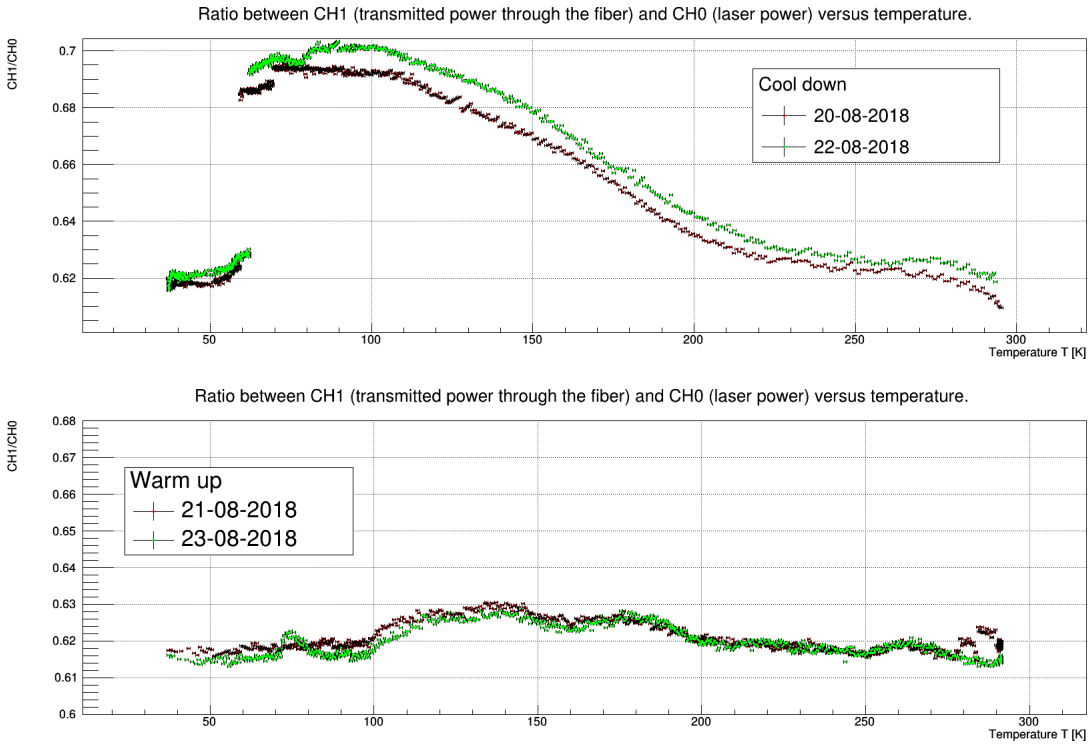

Figure 23: Transmittance of the set-up with two mating sleeves and a curled long fiber connecting them inside the cryostat during two cool downs and two warm ups plotted as a function of temperature.

Tests on the reliability of these results and measurements on the fibers and the mating sleeves' behaviour in the cold temperature are still ongoing.

3.2 Tackling signal losses due to a cold environment

As already mentioned before, ALPS IIc being an extreme precision experiment, a crucial step when testing sections of the experimental set-up is making sure that signal losses are minimized. With the filter bench set-up this step is critical: disentangling the effects brought about by different parts has proved itself to be a complicated task.
Previous tests carried out on the filter bench revealed that a drop in transmittance from $\sim 90\%$ to $\sim 60\%$ of this value occurred during a cool down of the cryostat, when only the two couplers were mounted on the filter bench, without the filter. The ultimate goal is to completely avoid this drop in transmittance: since the filter is absent in this set-up, this effect is to be attributed to an overall misallignment of the optical elements.
The reason for this drop in transmittance is suspected to be the titanium couplers' thermal shrinking. Due to the temperature gradient occurring during a cool down, the titanium couplers undergo thermal shrinking, bringing the optical fibers and the lenses closer to each other. Thus, the optical allignment reached when setting up the filter bench in the warm temperature is disrupted, simply because the laser light is not focused to the second fiber anymore. If this is really the case, these signal losses could be tackled by purposefully misaligning the optical system in the warm temperature, such that the thermal shrinking of the couplers occurring during the cool down makes the distance between the lenses and the fibers exactly coincident with the lenses' focal distance. The purposeful misalignment of the optical system is, however, a tricky task. The only way way to modify alignment is to act on the six screws on each coupler: we can't see the inner parts of the coupler, nor measure the distance between the lens and the fiber.
A simulation was carried out to understand if the drop in transmittance could really be due to the coupler's thermal shrinking. The model employed for the simulation coincides with the second half of the filter bench set-up. A gaussian laser beam, whose direction of propagation is parallel to the optical axis, hits a focusing lens, and at a distance L from this lens an optical fiber is present. This very simple model is used to compute the transmittance of this set-up as a function of L (the distance between the lens and the optical fiber)[22].

Features of the lens

Focal distance f[mm]	11
Maximum aperture A [mm]	5.5

Table 1: The coupler's lens features are shown.

The diameter of the gaussian laser beam is $a = 3$ mm. To correctly understand this, one has to remember that the simple model used for this simulation coincided with the second half the filter bench set-up. In the first half of this set-up, an optical fiber emits a gaussian laser beam with $NA = 0.14$, and shines it towards a lens with $f = 11$ mm. If one assumes that the distance between the first fiber and the first lens is equal to the focal distance f, the transmitted gaussian beam is propagating in parallel with the optical axis and its diameter is $a = 2f\tan(\theta_{acc}) = 2f\tan(\mathsf{arcsin}(NA)) \approx 3$ mm.

[22]It's useful to remind the features of the lens and the optical fiber.

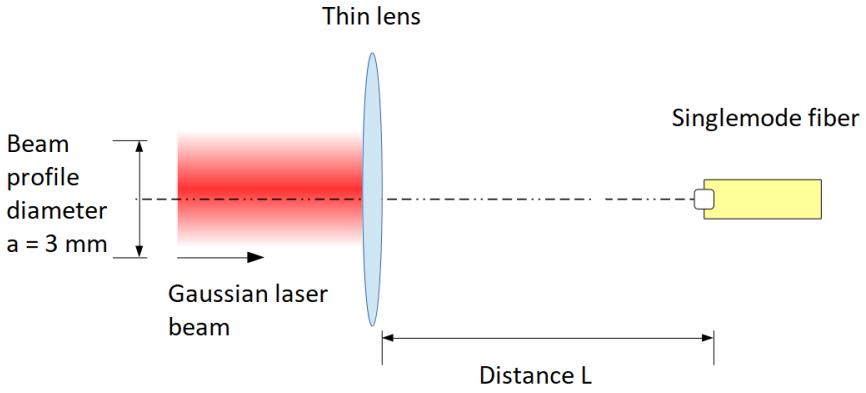

Figure 24: Drawing of the simple model used for the simulation.

Features of the optical fiber

Mode field diameter MFD [μm]	9.8
Core diameter h [μm]	8.0
Numerical aperture NA	0.14

Table 2: The optical fiber's lens are shown.

The distance L between the lens and the fiber is then varied between f - 1 mm and f + 1 mm, and for each of these values the transmittance of the set-up is computed.
The second step is to compute the distances L where the transmittance is equal to $\sqrt{0.6} \cdot 0.9$[23]. The width of the window in which the transmittance is above $\sqrt{0.6} \cdot 0.9 \approx 0.697$ is equal to $\Delta L = 102.6$ μm. The change of length in the coupler brings the lens and the coupler closer together. Thus, the final result of this simulation is that the transmittance of the set-up is equal to ~ 0.697 when the distance between the lens and the fiber decreases of $\Delta L/2 = 51.1$ μm from the focal distance f.
This numerical result needs to be compared with the change in length of the titanium coupler due to thermal shrinking. The change in length Δl of the titanium coupler is defined by

$$\frac{\Delta l}{l} = \alpha \Delta T \tag{10}$$

where l is the original length of the coupler, ΔT is the temperature gradient during the cool down and α is the coefficient of thermal expansion of titanium. Assuming that α does not depend on temperature[24], and knowing l and ΔT one can compute the expected Δl due to thermal shrinking. As the above table shows, the value for $\Delta L/2 = 51.1$ μm obtained with the simulation is compatible within a $\sim 16\%$ error with the length shrinkage

[23]The drop in transmittance observed during the tests on the filter bench set-up with only couplers present brings the total transmittance to 60% of a 90% transmittance value obtained at room temperature. This model incorporates only the second half of the filter bench set-up: the expected drop with only half of the set up is then from 90% to the square root of 60%.

[24]Actually the coefficient of thermal expansion depends from the temperature, and the previous formula in an approximation of the integral $\frac{\Delta l}{l} = \int_{T_i}^{T_f} \alpha(T) dT$ where T_i and T_f are the initial and the final temperatures. The computed thermal shrinkage (60.8 μm) is an upper limit of the real value, because the coefficient of thermal expansion $\alpha(T)$ is a decreasing function of T.

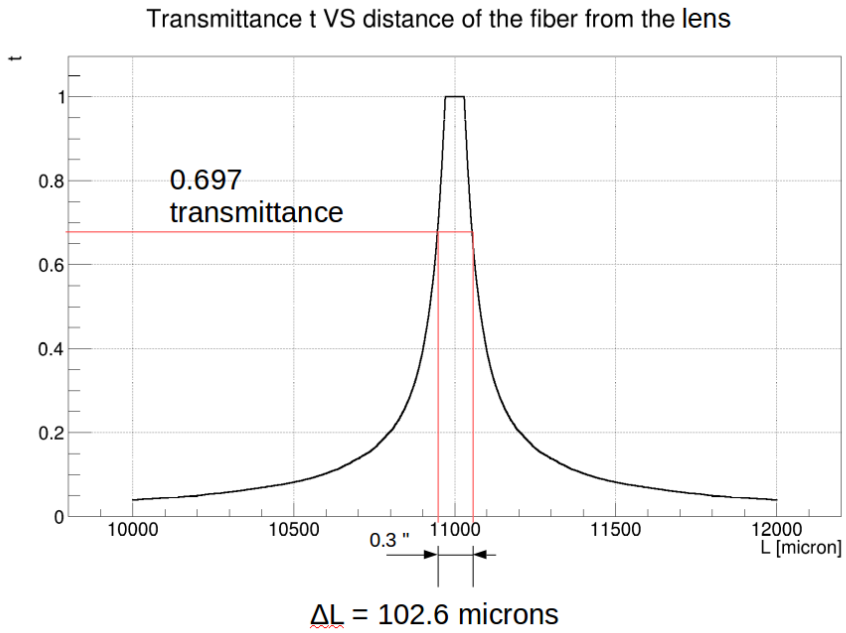

Figure 25: Transmittance of the model set-up as a function of the distance L between the lens and the fiber. The ΔL window is highlighted.

Simulation results

Coupler's length at room temperature l [mm]	27.9
Temperature gradient during a cool down ΔT [K]	257
Coefficient of thermal expansion of titanium at room temperature α [K^{-1}]	$8.5 \cdot 10^{-6}$
Expected shrinkage in coupler's length Δl [μm]	60.8

Table 3: This table summarises the main results of the simulation.

of the titanium coupler. Confirmation of this results is however needed: to demonstrate that the observed drop in transmittance is caused by the coupler's thermal shrinkage, one should repeat the tests on the filter bench with only couplers. When setting up the filter bench on the first flange on the cryostat, one should then purposefully select a distance between the couplers and the fibers closer to $f + \Delta L/2$ rather than to f. With this set-up, during the cool down, if the drop in transmittance of the previous observations was really caused by thermal shrinking of titanium, this same effect would decrease the distance between the couplers and the fiber to be closer to f, thus increasing the overall transmittance. However, as already mentioned before, setting up this measurement would not be easily feasible.

4 Conclusions

The experimental results summarized in this project show how optical elements employed for filtering black body photons respond to very cold temperatures. The anti-correlative behaviour between laser power and transmitted power observed when a filter bench set-up was employed can be explained by the laser's emission spectrum changing with laser power.

The responses of the two set-ups involving mating sleeves and optical fibers need further investigation. A simulation was carried out to explain an observed drop in transmittance from $\sim 90\%$ to $\sim 60\%$ of this value with a filter bench set-up in absence of the filter. A transmittance of $\sqrt{0.6} \cdot 0.9$ is reached by the simulated model when the distance between the lens and the fiber incorporated by the titanium coupler is $\Delta L/2 = 51.3$ μm less than the lens' focal distance $f = 11$ mm. This number is compatible with the thermal shrinkage the 27.9 mm long titanium coupler, $\Delta \mathrm{l} = 60.8$ μm. Thus, thermal shrinkage of the titanium couplers could cause this drop in transmittance.

References

[1] Axel Lindner, Andreas Ringwald, and Bela Majorovits. *Search for WISPs gains momentum.* 2018.

[2] Peter Graham, Igor Irastorza, Steven Lamoreaux, Axel Lindner, and Karl van Bibber. *Experimental Searches for the Axion and Axion-like Particles.* 2016.

[3] Baker et al. *The quest for axions and other new light particles.* 2013.

[4] Jan Dreyling-Eschweiler. *A super conducting microcalorimeter for low-ux detection of near-infrared single photons.* DESY, 2014.

[5] Bahre et al. *Any Light Particle Search II Technical Design Report.* DESY, 2013.

[6] ALPS WIKI.